Supporting Information

Interfacial Engineering-Induced Electronic State Modulation in Ru/MoS$_2$ Heterostructures for Efficient Hydrogen Evolution Reaction

Ning Wang,‡[abc] Yajing Zhang,‡[bce] Canhui Zhang,[abc] Xingkun Wang,[bce] Shuixing Dai,[abc] Minghua Huang*[a] and Heqing Jiang*[bce]

1. Experimental section

1.1 Materials characterization:

The sample morphologies were studied using scanning electron microscopy (SEM) characterized by Hitachi S-4800. Transmission electron microscopy (TEM) and high-resolution TEM (HRTEM) images were obtained by FEI Technai G2 F20 with working voltage of 200 KV, and element mapping analysis were conducted on Talos F200X with Super-X EDS system. X-ray photoelectron spectroscopy (XPS) was measured for the change of chemical states and the chemical composition of all products by Thermo ESCALAB 250Xi multifunctional imaging electron spectrometer. Using Si(111) double-crystal monochromator, the data collection were carried out in fluorescence mode using Lytle detector. All spectra were collected in ambient conditions. The crystal structure of all as-synthetized samples was characterized by XRD using a Bruker D8 Advance diffractometer (Cu Kα, λ = 1.54178Å). Raman spectroscopy carried out using a Thermo Fisher spectrometer.

1.2 Electrochemical measurements:

All electrochemical measurements were carried out in an alkaline solution (1 M KOH) standard three-electrode system using Interface 5000E electrochemical workstation (Gamry, USA) and CHI 660E electrochemical workstation (Chenhua, China). The different catalysts on CC (1 cm^2) were used directly as working electrode, while the graphite rod and Hg/HgO were used as counter and reference electrodes, respectively. The HER performances were measured via Linear sweep voltammetry (LSV) with a scan rate of 5 mV s^{-1} and the LSV curves were corrected by iR compensation automatically on the electrochemical workstation, and the obtained potentials were all converted to reversible hydrogen electrode (RHE) according to the equation: E$_{RHE}$=E$_{Hg/HgO}$+0.0591×pH+0.098. Electrochemical impedance spectroscopy (EIS) was tested from 0.01 Hz to 100kHz with 10 mV rms AC voltage at a potential of -1.0 V vs. RHE. The C$_{dl}$ values were measured through CV in the selected non-faradaic range with a series of different scan rates from 10 mV s^{-1} to 30 mV s^{-1}. The stability test was characterized via chronopotentiometry at a stationary current density of 500 mA cm^{-2} for 300 h without iR compensation.

1.3 DFT theoretical calculation:

The Vienna Ab Initio Package (VASP) was employed to perform all the density functional theory (DFT) calculations within the generalized gradient approximation (GGA) using the Perdew, Burke, and Enzerhof (PBE) formulation. The projected augmented wave (PAW) potentials were applied to describe the ionic cores and take valence electrons into account using a plane wave basis set with a kinetic energy cutoff of 500 eV. Partial occupancies of the Kohn–Sham orbitals were allowed using the Gaussian smearing method with a width of 0.05 eV. The electronic energy was considered self-consistent when the energy change was smaller than 10^{-5} eV. A geometry optimization was considered convergent when the force change was smaller than 0.05 eV/Å. Grimme's DFT-D3

methodology was used to describe the dispersion interactions. The vacuum spacing perpendicular to the plane of the structure is 20 Å. The Brillouin zone integral utilized the surfaces structures of 2×2×1 monkhorst pack K-point sampling. Finally, the adsorption energies(Eads) were calculated as Eads= Ead/sub -Ead -Esub, where Ead/sub, Ead, and Esub are the total energies of the optimized adsorbate/substrate system, the adsorbate in the structure, and the clean substrate, respectively.

The free energy was calculated using the equation:

G=Eads+ZPE-TS

where G, Eads, ZPE and TS are the free energy, total energy from DFT calculations, zero point energy and entropic contributions, respectively.

1.4 Experimental

1.4.1 Synthesis of MoS$_2$

MoS$_2$ was synthesized via a typical hydrothermal method. First, 1.236 g of ammonium molybdate [(NH$_4$)$_6$Mo$_7$O$_{24}$·4H$_2$O] and 2.284 g of thiourea (CH$_4$N$_2$S) were dispersed in 35 mL of deionized water and stirred continuously for 30 minutes. The resulting homogeneous solution was then transferred to a 50 mL Teflon-lined stainless-steel autoclave and maintained at 180 °C for 24 h. After the reaction, the solution was allowed to cool to room temperature, and the product was washed three times with deionized water and ethanol, followed by vacuum drying at 60 °C. Finally, the dried powder was sintered at 600°C under a nitrogen atmosphere for 2 h, with a heating rate of 2 °C/min.

1.4.2 Synthesis of Ru-MoS$_2$

First, 60 mg of MoS$_2$ was weighed and dispersed into 20 mL of deionized water, followed by ultrasonic treatment for 30 minutes and stirring at 800 rpm for 10 minutes. Then, the stirring speed was increased to 2000 rpm, and 600 μL of 25 mM RuCl$_3$ solution was added dropwise. The mixture was stirred continuously at 2000 rpm for 2 h. Afterward, the beaker was immersed in liquid nitrogen for rapid freezing, followed by vacuum freeze-drying. Finally, the dried powder was sintered at 600°C under a nitrogen atmosphere for 2 h, with a heating rate of 2 °C/min.

1.4.3 Synthesis of Ru-RuS$_2$/MoS$_2$

First, 60 mg of MoS$_2$ was weighed and dispersed into 20 mL of deionized water, followed by ultrasonic treatment for 30 minutes and stirring at 800 rpm for 10 minutes. Then, the stirring speed was increased to 2000 rpm, and 600 μL of 150 mM RuCl$_3$ solution was added dropwise. The mixture was stirred continuously at 2000 rpm for 2 hours. Afterward, the beaker was immersed in liquid nitrogen for rapid freezing, followed by vacuum freeze-drying. Finally, the dried powder was sintered at 600°C under a nitrogen atmosphere for 2 hours, with a heating rate of 2 °C/min.
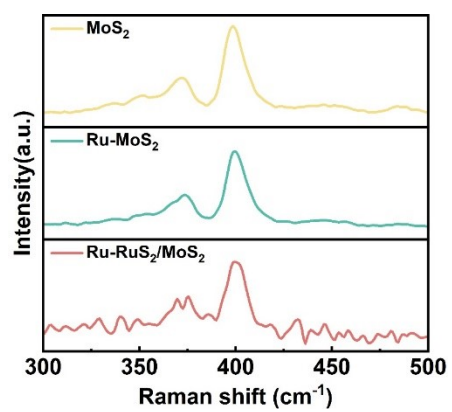
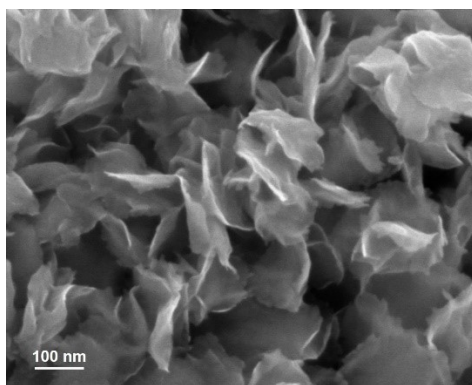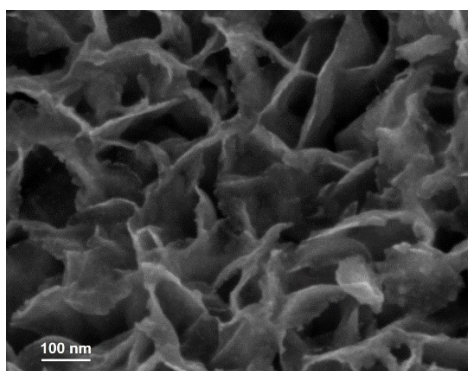Fig. S1 Raman spectra of MoS_2, Ru-MoS_2, and Ru-RuS_2/MoS_2.

Fig. S2 SEM image of MoS_2.

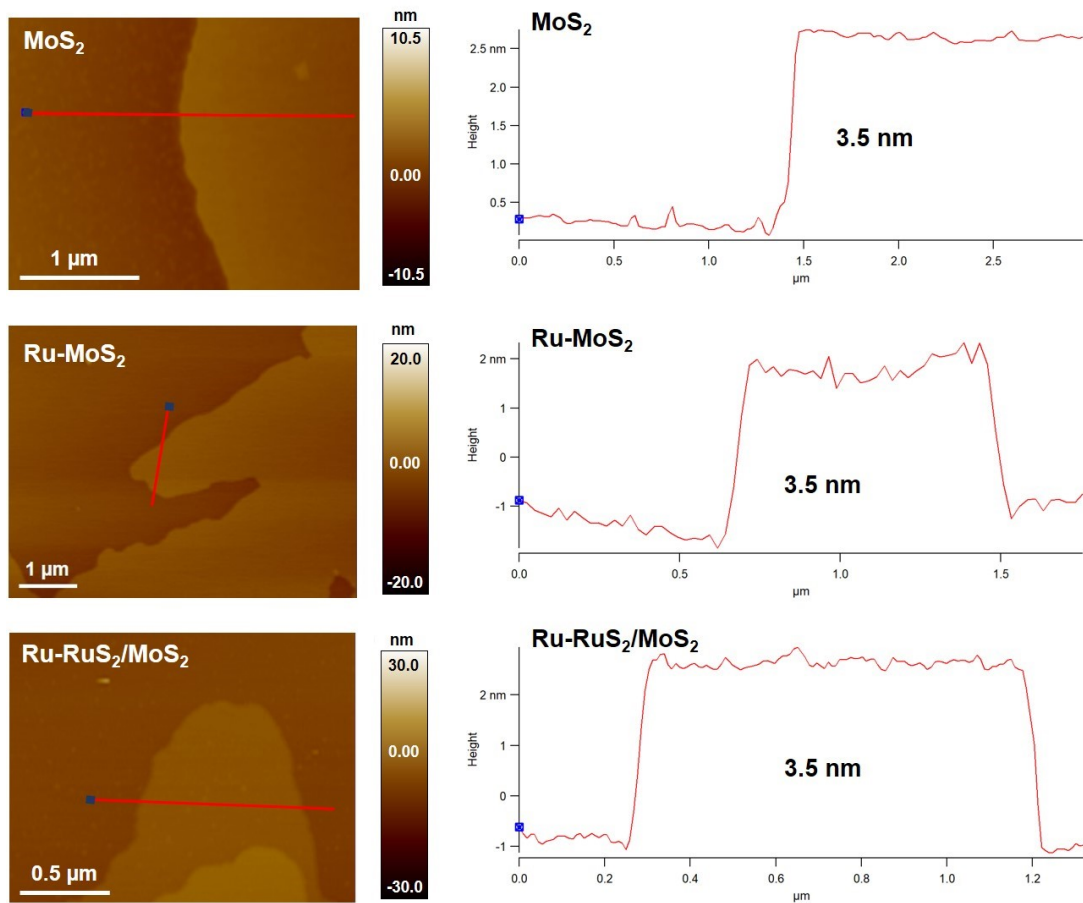Fig. S3 SEM image of Ru-RuS_2/MoS_2.

Fig. S4 Atomic force microscope (AFM) results of MoS_2, $Ru-MoS_2$ and $Ru-RuS_2/MoS_2$, respectively. The atomic force microscopy tests showed that the thicknesses of MoS_2, $Ru-MoS_2$ and $Ru-RuS_2/MoS_2$ catalysts are all approximately 3.5 nm. The results indicate that the activation of the inert plane is caused by heterojunction effects, rather than changes in MoS_2 thickness.
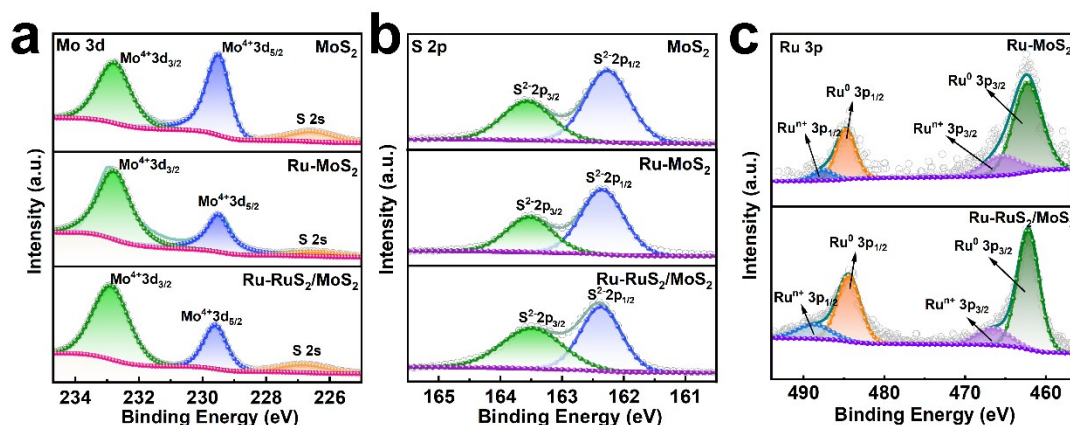
Fig. S5 Characterization of valence states and electronic structure. a) Mo 3d XPS spectra, b) S 2p XPS spectra of MoS_2, $Ru-MoS_2$ and $Ru-RuS_2/MoS_2$, and c) Ru 3d XPS spectra of $Ru-MoS_2$ and $Ru-RuS_2/MoS_2$.

The electronic properties and valence states of all samples were evaluated using X-ray photoelectron spectroscopy (XPS). The high-resolution XPS spectra of Mo 3d elucidated two characteristic Mo peaks centered at 232.9 eV and 229.6 eV, corresponding to Mo^{4+} $3d_{3/2}$ and Mo^{4+} $3d_{5/2}$, respectively (fig. S4a). In the S 2p spectrum (fig. S4b), the existence of the S^{2-} $2p_{3/2}$ and S^{2-} $2p_{1/2}$ can be confirmed, suported by the characteristic peaks at 163.5 eV and 162.4 eV in order. Notably, in the high-resolution XPS spectra of Ru 3p (fig. S4c), the characteristic peaks of Ru^{n+} $3p_{1/2}$ (488.75 eV) and Ru^{n+} $3p_{3/2}$ (466.5 eV) in $Ru-RuS_2/MoS_2$ are elevated positivie shift approximately 1 eV compared to the corresponding peaks in $Ru-MoS_2$, Ru^{n+} $3p_{1/2}$ (487.6 eV) and Ru^{n+} $3p_{3/2}$ (465.5 eV).
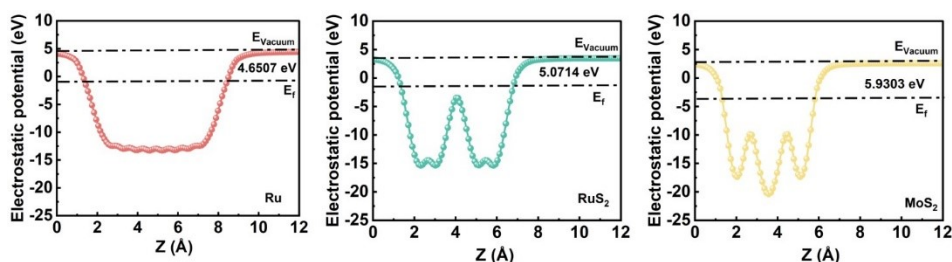

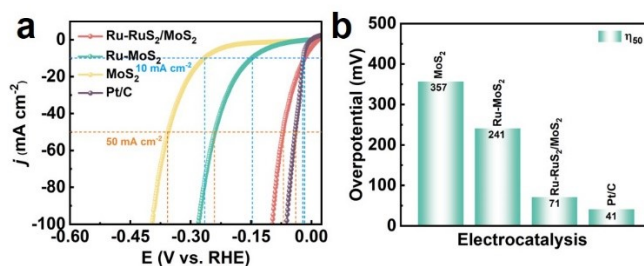Fig. S6 Work function calculations of Ru, RuS_2, and MoS_2.

Fig. S7 (a) LSV curves with a current density of up to 100 mA cm^{-2}. (b) The differences in catalyst performance can be observed more clearly in this figure.
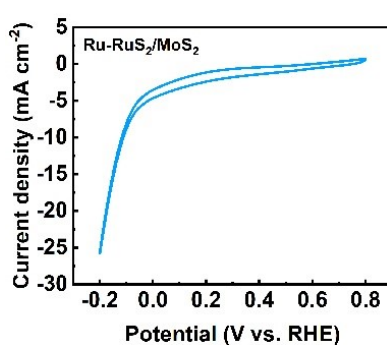

Fig. S8 CV curves of Ru-RuS$_2$/MoS$_2$ over a wide potential range. To determine the voltage range for measuring the electrochemical active surface area (ECSA) within the non-Faradaic region, we conducted cyclic voltammetry (CV) tests for Ru-RuS$_2$/MoS$_2$ across a broad voltage range. The CV results indicate that the non-Faradaic region is within the voltage range of 0.4 V to 0.5 V
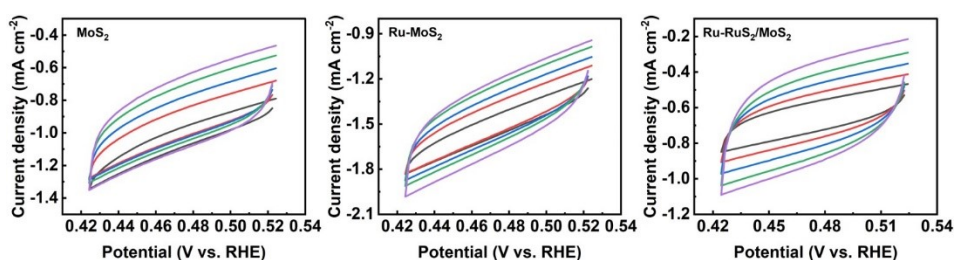

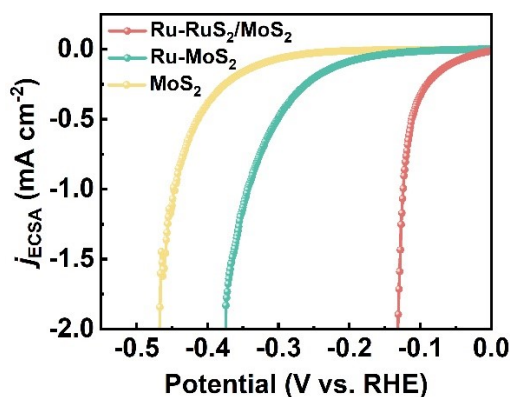Fig. S9 The C$_{dl}$ values were measured through CV in the selected non-faradaic range with a series of different scan rates from 10 mV s^{-1} to 30 mV s^{-1}

Fig. S10 HER polarization curves of MoS_2, Ru-MoS_2, and Ru-RuS_2/MoS_2 after normalizing by ECSA values.

The electrochemical active surface area (ECSA) was determined based on C_{dl} using the following formula:

$$ECSA = \frac{C_{dl}}{C_s}$$

in which an ideal planar electrode has a C_{dl} of 60 μF cm^{-2} defined as $Cs = 60$ μF cm^{-2}.

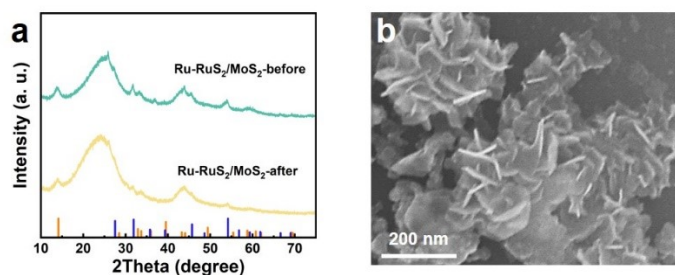Fig. S11 (a) XRD characterization of Ru-RuS_2/MoS_2 before and after stability testing and (b) SEM images of Ru-RuS_2/MoS_2 after stability testing. After stability testing, SEM analysis revealed that the morphology of the Ru-RuS_2/MoS_2 catalyst remained nanosheet-like; XRD analysis confirmed that the post-reaction Ru-RuS_2/MoS_2 catalyst retained its original structure. Note: After stability testing, the catalyst characterization was performed while the catalysts were affixed to carbon cloth, which is why the carbon cloth substrate can be observed in the SEM images. Additionally, the XRD analysis exhibited distinct carbon diffraction peaks, and due to the relatively low loading of the catalyst, the intensity of the characteristic peaks of the catalyst was notably diminished.
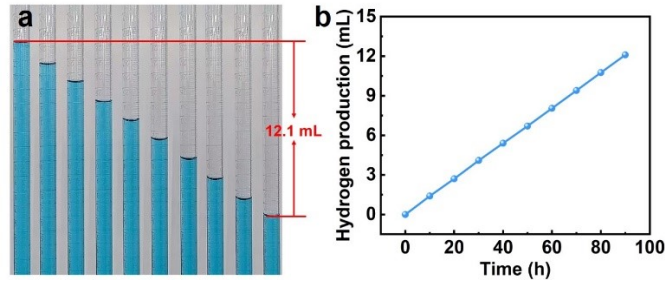
Fig. S12 Faradaic efficiency testing of the catalyst Ru-RuS$_2$/MoS$_2$: (a and b) the hydrogen production amount (recorded every ten minutes) measured in the experiment. We tested the Faradaic efficiency of Ru-RuS$_2$/MoS$_2$ at room temperature. Under a current of 20 mA, 12.1 mL of hydrogen gas was produced over 90 minutes (theoretically expected to be 12.51 mL). The calculation yields a Faradaic efficiency of 96.7%

The theoretical H$_2$ amount was calculated as follows.

$$n\left(H_2\right) = \frac{Q}{nF}$$

where Q is the charge through the electrode, n (H$_2$) is the number of moles of hydrogen produced, F is Faraday constant of 96,485 C mol^{-1}, and n is the number of transferred electrons during the water splitting (2 for HER).
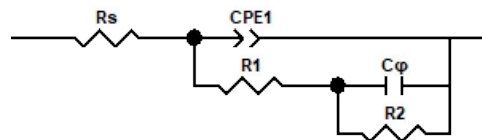

Fig. S13 The simulated equivalent circuit diagram, where the second set of parallel components, Cφ and R2, represents the hydrogen adsorption behavior on the catalyst surface. The physical meanings of Cφ and R2 correspond to the hydrogen adsorption capacitance and hydrogen adsorption resistance, respectively.
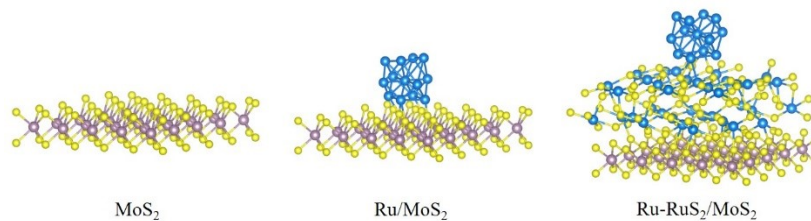

MoS$_2$　　　　Ru/MoS$_2$　　　　Ru-RuS$_2$/MoS$_2$

Fig. S14 The theoretical models of the optimized configurations of MoS$_2$, Ru-MoS$_2$, and Ru-

RuS$_2$/MoS$_2$.

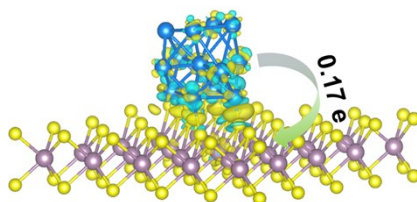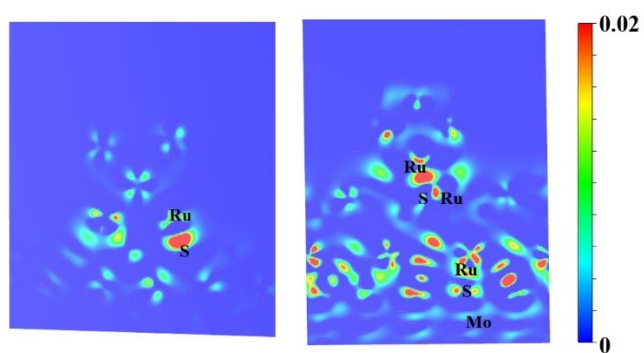Fig. S15 Charge density difference plot at the Ru-MoS$_2$ interface.

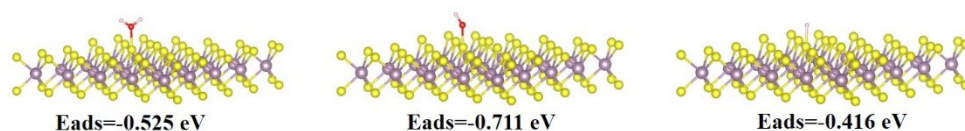Fig. S16 Visualized two-dimensional slices of the charge density for the Ru-MoS$_2$ and Ru-RuS$_2$/MoS$_2$ models.

Eads=-0.525 eV   Eads=-0.711 eV   Eads=-0.416 eV

Fig S17 Adsorption models and adsorption energies of MoS_2 for $*H_2O$, $*OH$, and $*H$.

Eads=-0.913 eV   Eads=-0.857 eV   Eads=-0.301 eV
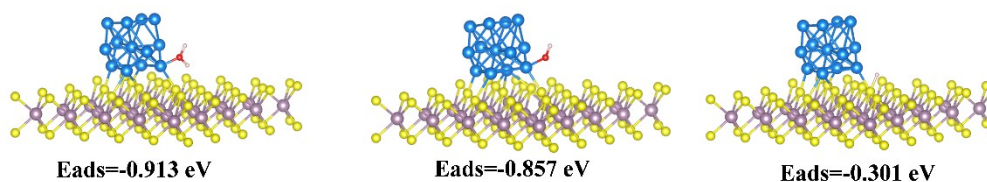
Fig S18 Adsorption models and adsorption energies of Ru-MoS_2 for $*H_2O$, $*OH$, and $*H$.

Eads=-1.247 eV   Eads=-1.035 eV   Eads=-0.197 eV

Fig S19 Adsorption models and adsorption energies of Ru-RuS_2/MoS_2 for $*H_2O$, $*OH$, and $*H$. Based on the DFT calculations, the Ru clusters in Ru-RuS_2/MoS_2 are considered the active sites for the adsorption of $*OH$, while the adsorption site for $*H$ is the sulfur atom on RuS_2, which is suitable for the hydrogen evolution reaction (HER). The catalytic process begins with the adsorption of water molecules onto the Ru clusters. Subsequently, the water molecules dissociate on the Ru clusters, resulting i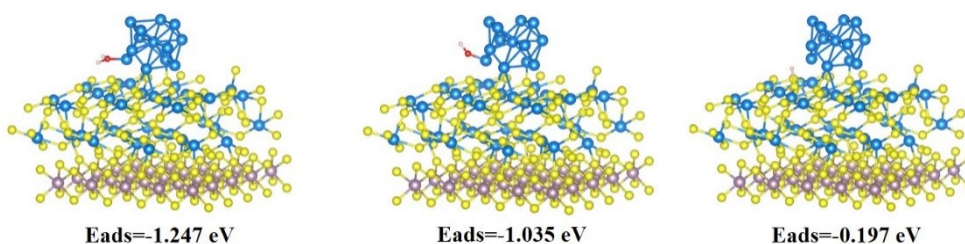n the formation of adsorbed H and $*OH$. Following this, $*H$ migrates to the nearest sulfur site on the Ru clusters, after which $*OH$ is removed, and protons from neighboring water molecules combine with $*H$, leading to the release of H_2.
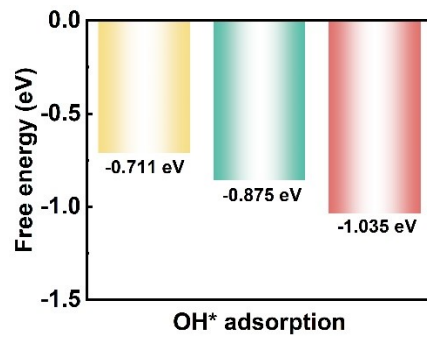
Fig S20 The *OH adsorption energies of MoS$_2$, Ru-MoS$_2$, and Ru-RuS$_2$/MoS$_2$.

Table S1 Comparison table of the overpotential of catalyst Ru-RuS$_2$/MoS$_2$ with other catalysts at 10 mA cm^{-2} under 1 M KOH conditions.

Catalysts	η_{10} (mV)	Reference
Ru-RuS$_2$/MoS$_2$	17	**This work**
Ru/RuO$_2$ SNSs	22	*Sci. Bull.*, 2022, **67**, 2103-2111.
RuSe$_2$	28	*Adv. Funct. Mater.*, 2024, 2404565.
Ru/np-MoS$_2$	30	*Nat. Commun.*, 2021, **12**, 1687.
Ru/Ni-MoS$_2$	32	*Appl. Catal. B*, 2021, **298**, 120557.
Ag500-MoS$_2$@Ni$_3$S$_2$/NF	33	*Adv. Sci.*, 2022, **9**, 2104774.
Ru-MoS$_2$@PPy	37	*Int. J. Hydrogen Energy*, 2022, **47**, 37850-37859.
MSOR1	43	*Adv. Funct. Mater.*, 2023, **33**, 2210939.
Ru$_{0.10}$@2H-MoS$_2$	51	*Appl. Catal. B*, 2021, **298**, 120490.
Ru$_2$@MoS$_2$-85%/CFP	54	*Chem. Eng. J.*, 2024, **489**, 151295.
Ni$_3$S$_2$/MoS$_2$	68	*ACS Appl. Mater. Interfaces*, 2021, **13**, 53262-53270.
R-MoS$_2$@NF	71	*Adv. Mater.*, 2018, **30**, 1707105.
Ni$_3$S$_2$@BL MoS$_2$	78	*Adv. Mater.*, 2022, **34**, 2202195.
N-doped MoS$_2$/Ti$_3$C$_2$	80	*Inorg. Chem.*, 2021, **60**, 9932-9940.
Ni-Sv-MoS$_2$	101	*Small*, 2022, **18**, 2203173.
Ru$_1$@D-MoS$_2$	107	*Small*, 2023, **19**, 2300807.
Ru@SvMoS$_2$	125	*Appl. Surf. Sci.*, 2024, **671**, 160704.

Table S2 The fitted parameters of the EIS data of Ru-RuS$_2$/MoS$_2$, Ru-MoS$_2$ and MoS$_2$ for HER.

Catalyst	η (mV)	R_s (Ω)	T (F s^{n-1})	R_1 (Ω)	R_2 (Ω)	C_φ (F)
Ru-RuS$_2$/MoS$_2$	-0.076	3.975	0.007892	5.87	95.66	0.00059219
	-0.126	3.959	0.007723	2.74	32.93	0.00084742
	-0.176	4.061	0.006332	4.172	11.33	0.00097138
	-0.226	4.104	0.005605	3.265	5.627	0.001046
	-0.276	4.012	0.005646	1.684	4.464	0.00095652
	-0.326	3.833	0.007197	1.134	3.744	0.0010224
	-0.376	4.13	0.004379	1.873	1.631	0.0012298
Ru-MoS$_2$	-0.076	5.393	0.007858	6.569	179	0.00072887
	-0.126	5.359	0.010697	5.088	81.86	0.0014114
	-0.176	5.327	0.009165	2.935	36.68	0.0023306
	-0.226	5.305	0.006872	3.353	19.35	0.0014526
	-0.276	5.234	0.005782	2.373	13.28	0.00067906
	-0.326	5.176	0.005759	1.767	9.108	0.0006884
	-0.376	5.11	0.006763	1.451	6.543	0.00078052
MoS$_2$	-0.076	2.874	0.005598	2.519	298.4	0.0011923
	-0.126	2.868	0.006253	1.865	233	0.0013774
	-0.176	2.864	0.00715	1.359	148.2	0.0016662
	-0.226	2.865	0.007897	1.066	53.4	0.0021791
	-0.276	2.876	0.007931	0.91686	15.02	0.0028858
	-0.326	2.879	0.008035	0.72777	6.246	0.0036727
	-0.376	2.885	0.007954	0.58041	3.823	0.00443